

Case C3.1: Turbulent Flow over a Multi-Element MDA Airfoil

Masayuki Yano* and David L. Darmofal†

Aerospace Computational Design Laboratory, Massachusetts Institute of Technology

I. Code Description

ProjectX is a high-order, adaptive discontinuous Galerkin finite element solver. The DG discretization uses Roe’s approximate Riemann solver¹ for the inviscid numerical flux, Bassi and Rebay’s second discretization (BR2)² for the viscous numerical flux, and Oliver’s asymptotically dual-consistent discretization³ for the RANS source term. Modifications have been made to the Spalart-Allmaras turbulence model⁴ as described by Oliver⁵ to improve robustness of the RANS model for higher-order discretizations. (The model incorporates few additional modifications by Modisette.⁶)

The solution to the discretized system is obtained using a Newton-based nonlinear solver with pseudo-time continuation and a line search on unsteady residual that explicitly controls the accuracy of time integration.^{6,7} The combination improves solver robustness, particularly through initial transients and on coarse meshes. The linear system arising in each pseudo-time step is solved using GMRES,⁸ preconditioned with an in-place block-ILU(0) factorization⁹ with minimum discarded fill reordering and $p = 0$ algebraic coarse correction.¹⁰

An output-based, anisotropic simplex adaptation algorithm is used to control the discretization error.¹¹ The algorithm iterates toward a mesh that minimizes the output error for a given number of degrees of freedom. The anisotropic adaptation decisions are entirely driven by the behavior of an output-based *a posteriori* error estimate; thus, the method handles any discretization order, naturally incorporates both the primal and adjoint solution behaviors, and robustly treats irregular features. The output error estimate uses the dual-weighted residual (DWR) method of Becker and Rannacher.¹² A new mesh that conforms to the metric request is generated using using BAMG (Bidimensional Anisotropic Mesh Generator),¹³ and higher-order, globally curved meshes are constructed through linear elasticity.³

II. Case Description

II.A. Flow Condition

This case considers turbulent flow over a three-element MDA 30P-30N airfoil, with a freestream Mach number of $M_\infty = 0.2$, an angle of attack of $\alpha = 16^\circ$, and a Reynolds number based on chord (in the retracted configuration) of $Re_c = 9 \times 10^6$. The dynamic viscosity is assumed to adhere to Sutherland’s law, the Prandtl number is set to $Pr = 0.71$, and the freestream turbulence level is set to $\rho_\infty \tilde{\nu}_\infty = 5.0 \rho_\infty \nu_\infty$.

II.B. Domain Specification

A square outer domain with the half-edge length of $R = 30000c$ is used for this case (i.e. the square is $60000c \times 60000c$). To minimize the effect of the farfield boundary location for this high-lift configuration, the flux at farfield boundaries is determined using the Roe flux in which the exterior state is set to the freestream conditions (instead of specifying the stagnation quantities and flow angle at the inflow and the static pressure at the outflow).¹⁴

*Doctoral candidate, 77 Massachusetts Ave. 37-442, Cambridge, MA, 02139, myano@mit.edu

†Professor, 77 Massachusetts Ave. 37-451, Cambridge, MA, 02139, darmofal@mit.edu

II.C. Convergence Criterion

The ℓ^2 norm of the DG residual of non-dimensionalized Navier-Stokes equations is used to monitor convergence to the steady state. Our solver operates on non-dimensionalized variables

$$\rho^* = \frac{\rho}{\rho_\infty}, \quad u^* = \frac{u}{\|V_\infty\|}, \quad v^* = \frac{v}{\|V_\infty\|}, \quad p^* = \frac{p}{\rho_\infty \|V_\infty\|^2}, \quad e^* = \frac{e}{\|V_\infty\|^2},$$

$$R^* = \frac{R}{c_v}, \quad T^* = \frac{T}{\|V_\infty\|^2/c_v}, \quad \text{and} \quad \mu^* = \frac{\mu}{\rho_\infty L_\infty V_\infty}.$$

The DG residual is computed against the Lagrange test functions with equidistributed nodes, and the ℓ^2 norm of the residual is converged to 1×10^{-9} . (Note that the solver time would not be significantly influenced for any reasonable choice of the tolerance (say $< 1 \times 10^{-7}$), as we achieve Newton convergence in this regime. With the specified non-dimensionalization, the difference between the ℓ^2 residual and the mass residual is well within this offset.)

II.D. Hardware Specification

All computations are performed in serial on a Linux machine with an Intel i7-2600 processor and 16 Gbytes of RAM. The machine produces a Taubench time of 6.60 seconds.

II.E. Residual Timing

The time for performing a single dof = 250,000 residual evaluation, including the full Jacobian construction for the implicit solver, is summarized in Table 1. The residual evaluation is performed on a 22097-element mesh and the times are scaled to 250,000 degrees of freedom.

p	time (work unit)
1	4.29
2	3.48
3	3.76

Table 1. dof = 250,000 residual evaluation time (including the full Jacobian construction).

II.F. Initial Mesh

The initial mesh used for this case is shown in Figure 1. The airfoil geometry is represented using $q = 3$ simplex elements. The mesh does not have any refinement in the boundary layer region and is unsuited for RANS calculation. Our objective is to demonstrate a fully-automated transition to a RANS mesh using the adaptive algorithm. After each mesh refinement, the geometry representation is refined by re-sampling from a fine cubic spline defining the three-element MDA airfoil geometry.

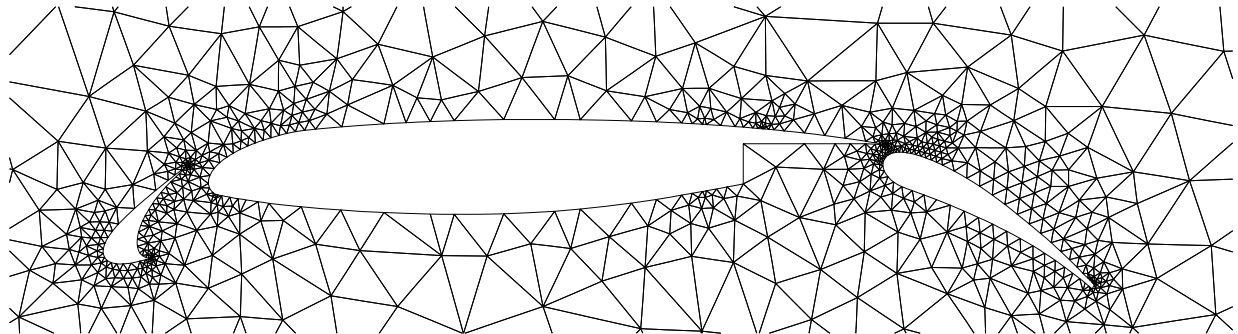


Figure 1. The initial mesh (2343 elements).

II.G. Adaptation Procedure and Data Reported

For each solution order p , the numbers of degrees of freedom considered are:

$$\begin{aligned} p = 1, & \quad \text{dof} = \{15000, 30000, 60000, 90000, 120000\} \\ p = 2, & \quad \text{dof} = \{30000, 60000, 90000, 120000\} \\ p = 3, & \quad \text{dof} = \{60000, 90000, 120000\}. \end{aligned}$$

For each p -dof combination, a family of optimized meshes are generated using our anisotropic simplex mesh adaptation algorithm.¹¹ The output adapted is the drag on the airfoil.

Similar to the transonic RANS flow considered in C2.2, it is difficult to converge the nonlinear problems arising from the $p > 1$ distributions on coarse meshes with no boundary layer resolution. To overcome the convergence difficulty, we perform the initial transition from the ‘‘Euler’’ mesh shown in Figure 1 to a coarse RANS mesh using a $p = 1$ discretization. Then, we start the adaptation sequence for the $p > 1$ discretizations starting from the coarse RANS mesh.

The c_d error variation during this initial transition process is shown in Figure 2. Starting from the initial mesh shown in Figure 1, nine $p = 1$, dof = 15,000 adaptation iterations are performed to obtain a coarse RANS mesh shown in Figure 3(a). On this coarse mesh, not all flow features are resolved; for instance, the lack of solution resolution in the lower side of the flap is apparent, and the drag error is over 80 counts. However, this mesh provides sufficient resolution for the $p = 2$ adaptation sequence to be started and carried out in a reliable manner. Nine additional $p = 2$, dof = 30,000 adaptation iterations results in a coarse $p = 2$ mesh shown in Figure 3(b). While the mesh is still coarse, the mesh is sufficient to provide the drag accuracy of 3 counts. Note that the adaptation targets select off-body features, such as the wake from the slat that interacts with the main element, before some on-body features, such as the boundary layer on the lower side of the main element.

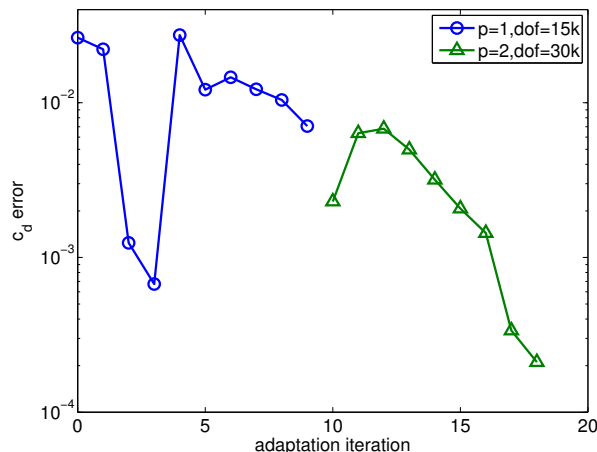


Figure 2. The drag coefficient error history in the Euler-to-RANS mesh transition.

As in Case 1.1, the performance of each p -dof is assessed by averaging the error obtained on five realization of meshes in the family. The time reported is the total time required to reach the first realization of the p -dof-optimized mesh starting from the initial mesh shown in Figure 1; this includes multiple flow solves and adaptation overhead. For example, the time to perform the entire 18 adaptation cycles is reported for the $p = 2$, dof = 30,000 case, whose drag error history is shown in Figure 2. (See the description provided in Case 1.1 for details on the error assessment procedure.)

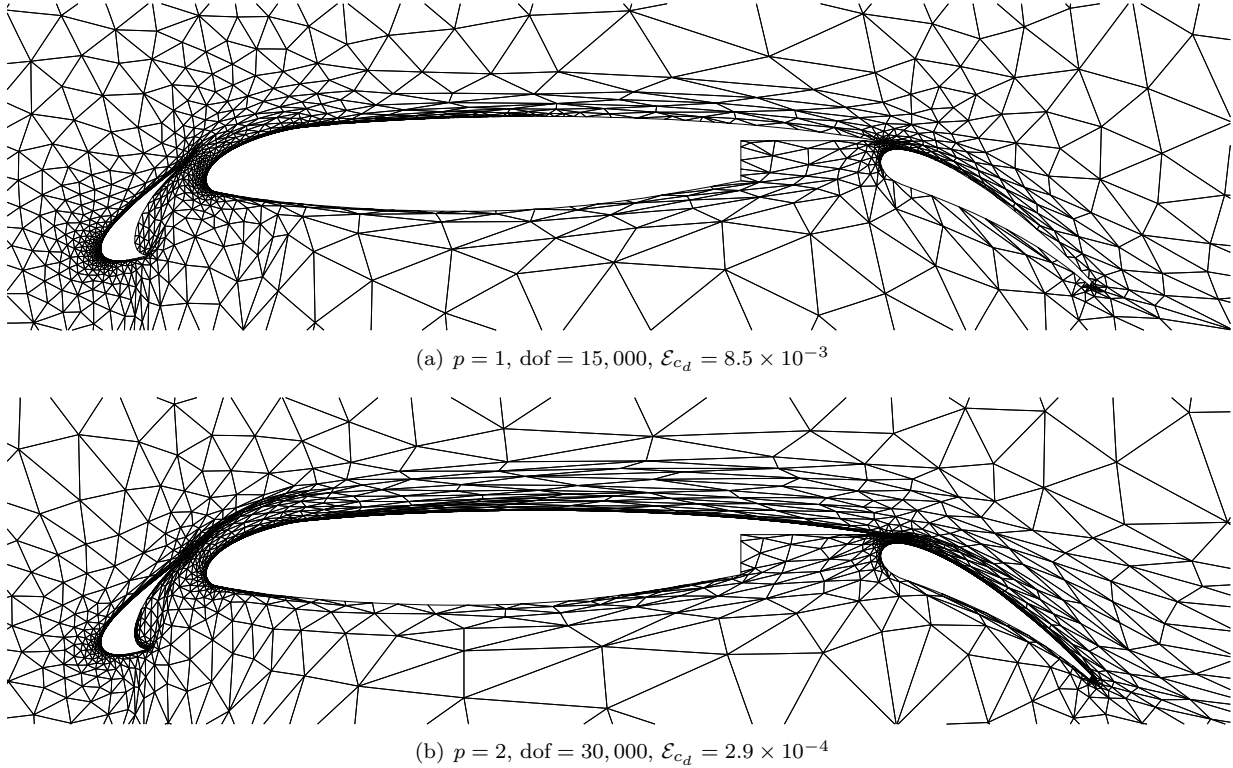


Figure 3. Coarse $p = 1$ and $p = 2$ meshes obtained after the initial transition.

III. Results

III.A. Error Convergence

The reference solution is obtained using the c_d -adapted $p = 3$, dof = 250000 discretization. The reference c_d and c_l values are

$$c_d = 0.047112 \pm 2 \times 10^{-6}$$

$$c_l = 4.1697,$$

where the error estimates are based on the adjoint-based error estimates and the fluctuation in the output values for this family of optimized meshes.

Figure 4(a) shows the drag error against the number of degrees of freedom. The $p > 1$ discretizations outperforms the $p = 1$ discretization for the entire range of degrees of freedom considered. At 120000 degrees of freedom, the $p = 1$ discretization still produces c_d error of several drag counts, whereas the $p = 2$ discretization requires less than 30,000 degrees of freedom to achieve a lower error level. The superiority of the higher-order discretizations is likely due to their ability to effectively convect information about the flow from the slat downstream to the flap. Figure 4(b) shows that the higher-order discretizations are also more efficient than the $p = 1$ discretization in terms of the work unit. In the range of accuracy required for a high-fidelity engineering application (say the c_d error of 1.0 to 0.1 counts), the $p = 2$ discretization is the most efficient discretization both in terms of the numbers of degrees of freedom and the work unit.

The lift results, shown in Figure 4(c), also confirm that the $p > 1$ discretizations outperform the $p = 1$ discretization for this high-lift configuration. The lift results are noisier than the drag results, perhaps because our meshes are drag-optimized. Our experience suggests that a stronger refinement along stagnation streamlines is necessary for accurate lift calculation than drag.

III.B. Adapted Meshes

Examples of drag-adapted meshes are shown in Figure 5. Various features in the primal and adjoint solutions are resolved through adaptive refinement. Adaptation targets not only the boundary layers, but also the

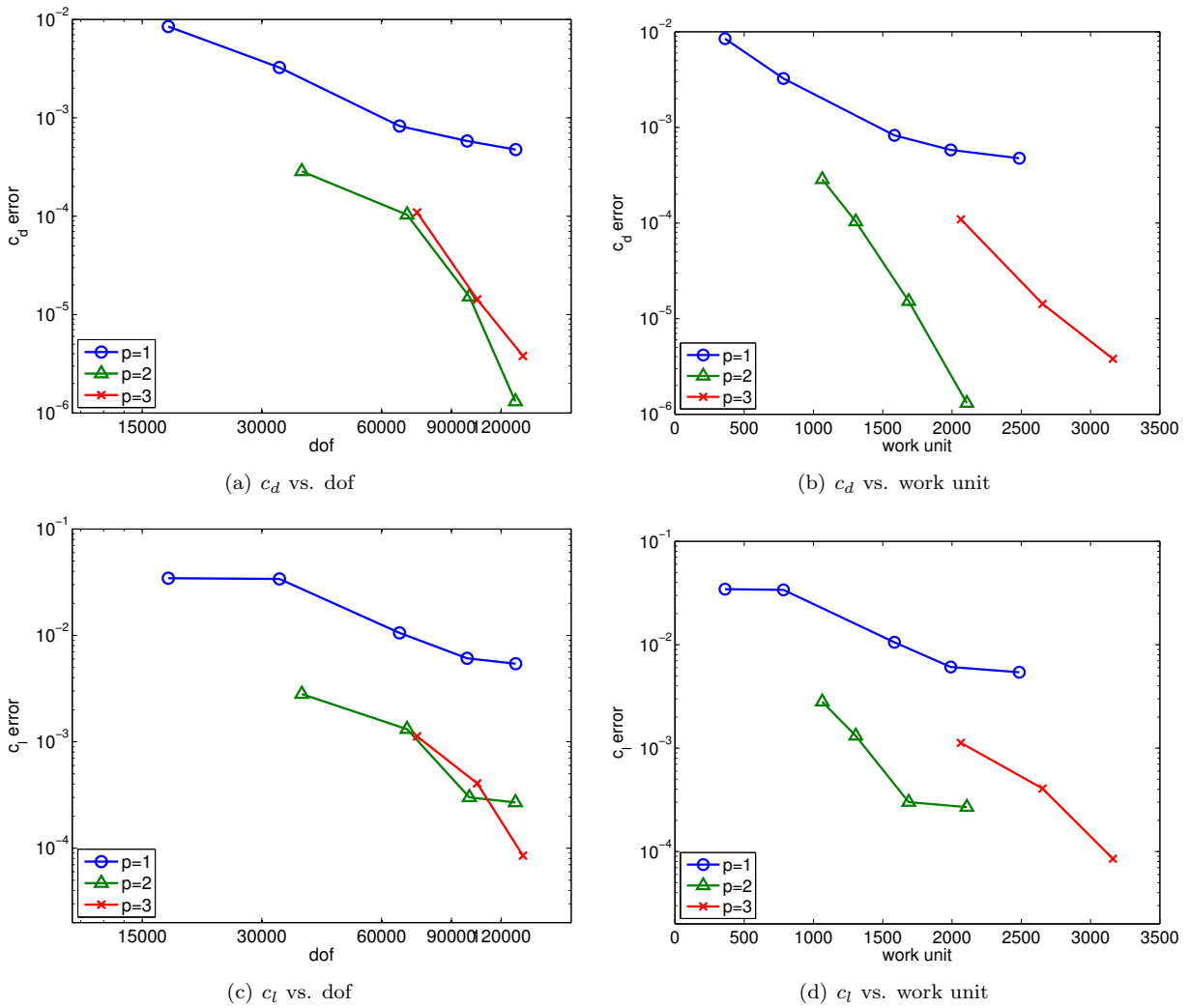
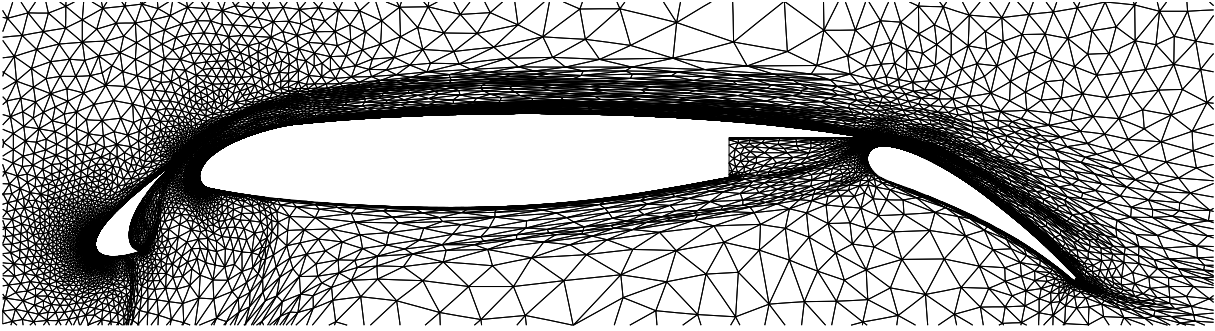


Figure 4. Error convergence.

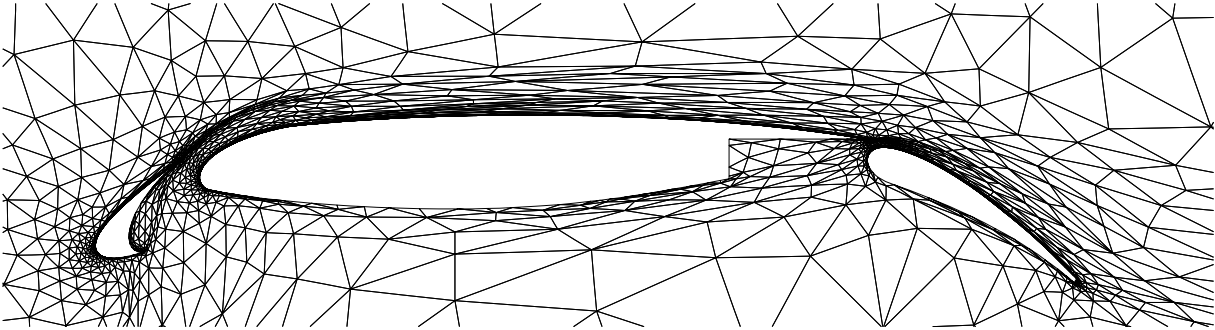
off-body features, such as wakes, that are crucial to accurately characterizing the interactions between the three elements of the high-lift airfoil (e.g. the main element wake interacting with the flap); the adjoint-based adaptation quantifies the importance of these interactions with respect to the output of interest and adapt as necessary.

Comparison of the $p = 1$, dof = 120,000 mesh (Figure 5(a)) and the $p = 2$, dof = 30,000 mesh (Figure 5(b)) shows the differences in the meshes required to compute the drag accurately to several counts. The $p = 2$ mesh is much sparser in the off body regions. The boundary layer in the lower side of the main element and the flap are also not resolved using on the $p = 2$ mesh; nevertheless, the $p = 2$ discretization achieves a lower drag error on this coarse mesh than the $p = 1$ discretization on a much finer mesh.

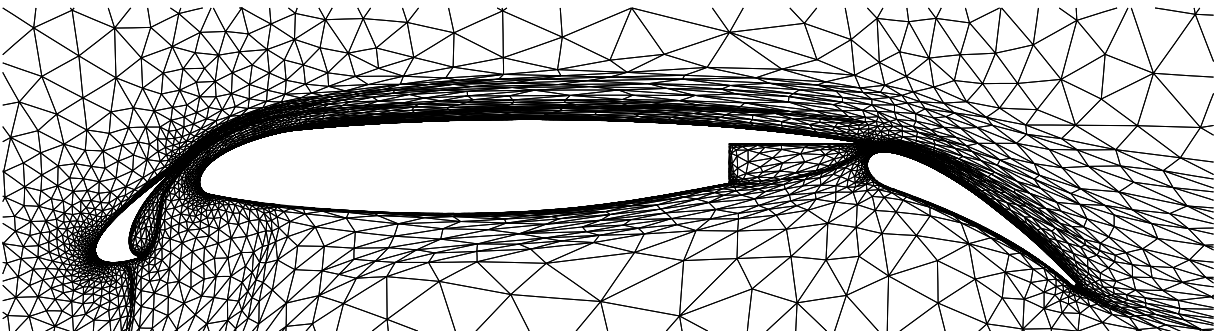
Comparison of the $p = 2$, dof = 30,000 mesh (Figure 5(b)) and the $p = 2$, dof = 120,000 mesh (Figure 5(c)) shows how the mesh evolves to achieve a lower error. The close up of the various regions of the $p = 2$, dof = 120,000 mesh is shown in Figure 6. The close up of the slat region and the flap region reveals anisotropic refinement of the wakes to effectively capture the interaction among the multiple elements of the airfoil. The farfield view shows that the adjoint-based refinement results in the refinement of both the wake and the stagnation streamline. The comparison of the mesh and a few components of the solution shown in Figure 7 clearly shows how the meshes generated are specifically designed for this flow.



(a) $p = 1$, dof = 120,000, $\mathcal{E}_{c_d} = 4.8 \times 10^{-4}$



(b) $p = 3$, dof = 30,000, $\mathcal{E}_{c_d} = 2.9 \times 10^{-4}$



(c) $p = 3$, dof = 120,000, $\mathcal{E}_{c_d} = 1.3 \times 10^{-6}$

Figure 5. Select adapted meshes.

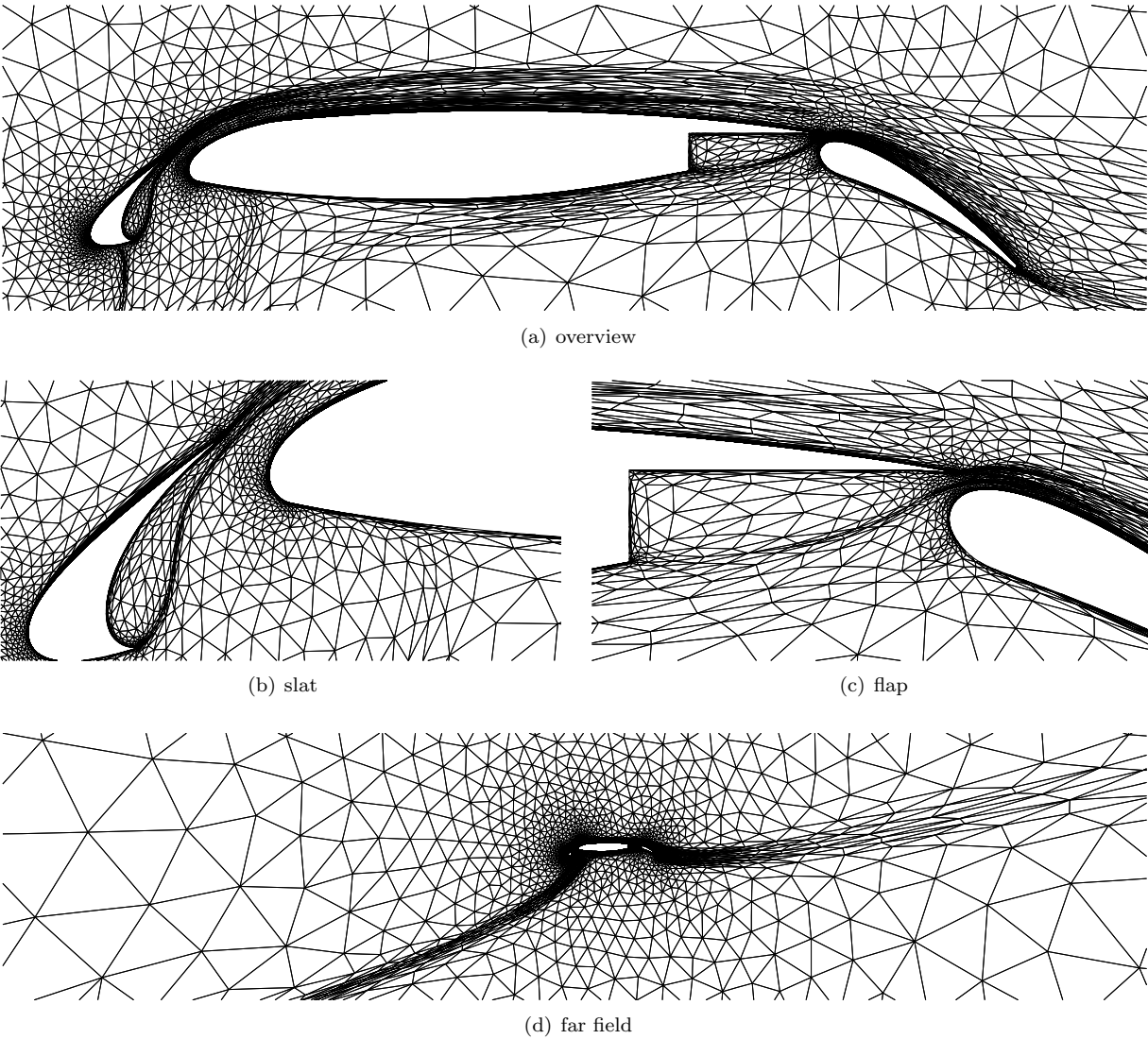


Figure 6. An example of adapted mesh. ($p = 2$, dof = 120000)

III.C. Surface Quantity Distributions

The pressure and skin coefficient distributions obtained on a $p = 3$, dof = 120,000 mesh are shown in Figure 8. While the c_p distribution is smooth, the c_f distribution is not as smooth as one might expect based on the low c_d error. In particular, the c_f distribution on the lower side of the flap is noisy. This may be due to the use of fully-unstructured simplex elements with high aspect ratio (and a large maximum angle); we expect the c_f distribution on a structured, quadrilateral mesh that achieve a similar error level to be much smoother.

Acknowledgments

The authors would like to thank the entire ProjectX team for the many contributions that enabled this work. Special thanks goes to Dr. Steven Allmaras for insightful discussions that led to improved robustness of the RANS-SA solver. This work was supported by the Singapore-MIT Alliance Fellowship in Computational Engineering and The Boeing Company with technical monitor Dr. Mori Mani.

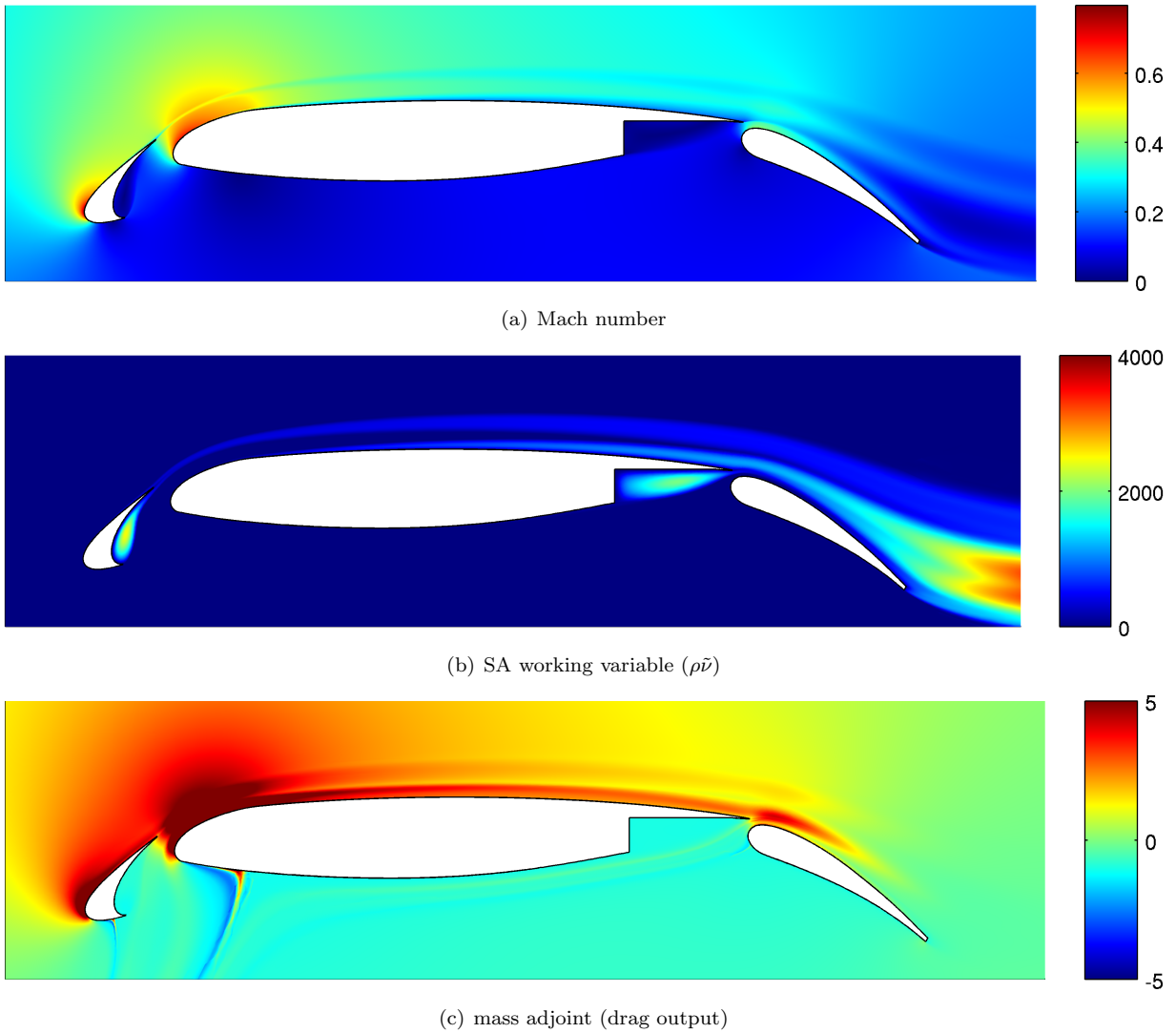


Figure 7. The Mach number, the SA working variable, and the mass adjoint for the drag output.

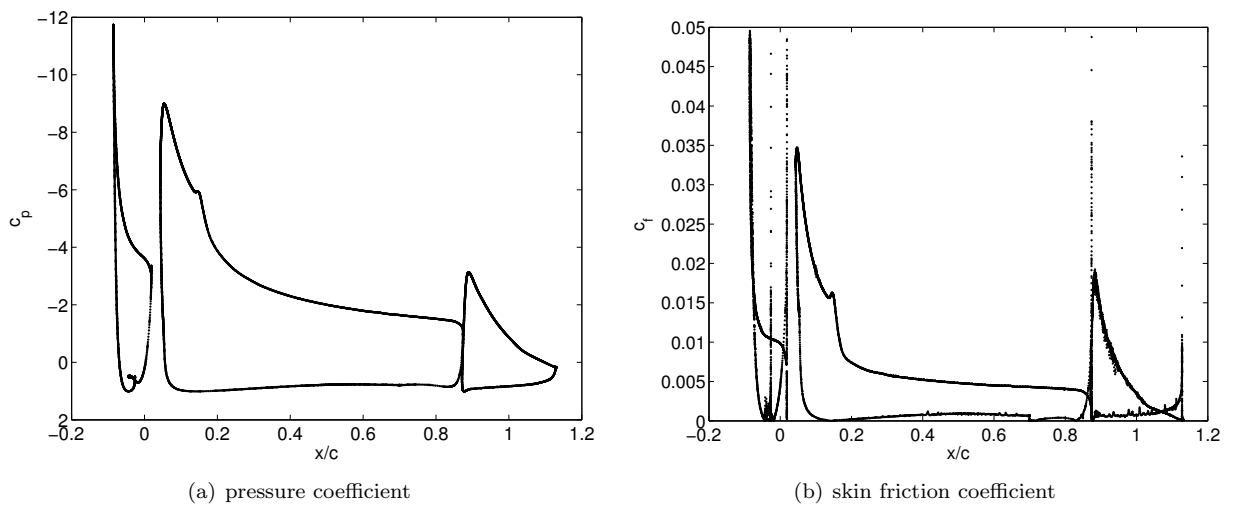


Figure 8. The pressure and skin friction coefficient distributions.

References

- ¹P. L. Roe, Approximate Riemann solvers, parameter vectors, and difference schemes, *J. Comput. Phys.* 43 (2) (1981) 357–372.
- ²F. Bassi, S. Rebay, GMRES discontinuous Galerkin solution of the compressible Navier-Stokes equations, in: K. Cockburn, Shu (Eds.), *Discontinuous Galerkin Methods: Theory, Computation and Applications*, Springer, Berlin, 2000, pp. 197–208.
- ³T. A. Oliver, A higher-order, adaptive, discontinuous Galerkin finite element method for the Reynolds-averaged Navier-Stokes equations, PhD thesis, Massachusetts Institute of Technology, Department of Aeronautics and Astronautics (Jun. 2008).
- ⁴P. R. Spalart, S. R. Allmaras, A one-equation turbulence model for aerodynamics flows, AIAA 1992-0439 (Jan. 1992).
- ⁵T. Oliver, D. Darmofal, Impact of turbulence model irregularity on high-order discretizations, AIAA 2009-953 (2009).
- ⁶J. M. Modisette, An automated reliable method for two-dimensional Reynolds-averaged Navier-Stokes simulations, PhD thesis, Massachusetts Institute of Technology, Department of Aeronautics and Astronautics (2011).
- ⁷M. Yano, J. M. Modisette, D. Darmofal, The importance of mesh adaptation for higher-order discretizations of aerodynamic flows, AIAA 2011-3852 (Jun. 2011).
- ⁸Y. Saad, M. H. Schultz, GMRES: A generalized minimal residual algorithm for solving nonsymmetric linear systems, *SIAM Journal on Scientific and Statistical Computing* 7 (3) (1986) 856–869.
- ⁹L. T. Diosady, D. L. Darmofal, Preconditioning methods for discontinuous Galerkin solutions of the Navier-Stokes equations, *J. Comput. Phys.* 228 (2009) 3917–3935.
- ¹⁰P.-O. Persson, J. Peraire, Newton-GMRES preconditioning for discontinuous Galerkin discretizations of the Navier-Stokes equations, *SIAM J. Sci. Comput.* 30 (6) (2008) 2709–2722.
- ¹¹M. Yano, D. Darmofal, An optimization framework for anisotropic simplex mesh adaptation: application to aerodynamic flows, AIAA 2012-0079 (Jan. 2012).
- ¹²R. Becker, R. Rannacher, An optimal control approach to a posteriori error estimation in finite element methods, in: A. Iserles (Ed.), *Acta Numerica*, Cambridge University Press, 2001.
- ¹³F. Hecht, Bamg: Bidimensional anisotropic mesh generator, <http://www-rocq1.inria.fr/gamma/cdrom/www/bamg/eng.htm> (1998).
- ¹⁴S. R. Allmaras, V. Venkatakrishnan, F. T. Johnson, Farfield boundary conditions for 2-d airfoils, AIAA 2005-4711 (2005).